A New Analytical Framework to Investigate the Precipitation Kinetics of Discharge Products in Li-S Batteries

Peer-reviewed author version

CONDE REIS, Albin; HAMED, Hamid; YARI, Saeed; VRANKEN, Thomas; D'HAEN, Jan; HARDY, An; REDDY, Naveen; Pang, Quanquan & SAFARI, Momo (2025) A New Analytical Framework to Investigate the Precipitation Kinetics of Discharge Products in Li-S Batteries. In: Small,.

DOI: 10.1002/smll.202503796
Handle: http://hdl.handle.net/1942/46612

A New Analytical Framework to Investigate the Precipitation Kinetics of Discharge Products in Li-S Batteries

Albin Conde Reis, [1,2,3] Hamid Hamed, [1,2,3] Saeed Yari, [1,2,3] Thomas Vranken, [1,2,3] Jan D'Haen, [1,3] An Hardy, [1,2,3] Naveen Reddy, [1,4] Quanquan Pang,[5] Mohammadhosein Safari *[1,2,3]

[1]*Institute for Materials Research (IMO-imomec), UHasselt, Martelarenlaan 42, Hasselt, 3500 Belgium*

[2] *Energyville, Thor Park 8320, Genk, 3600 Belgium*

[3] *IMEC Division IMOMEC, Diepenbeek, 3590 Belgium*

[4] *IMEC, Kapeldreef 75, Leuven, 3001 Belgium*

[5] *Beijing Key Laboratory for Theory and Technology of Advanced Battery Materials, School of Materials Science and Engineering, Peking University, Beijing 100871, China*

Polysulfides are central to the inner-workings of lithium-sulfur (Li-S) batteries. They are responsible for the inertia and snowballing effects at play on the dynamics of the battery, among those, the infamous shuttle effect. For this reason, it is very challenging to establish analytical tools for quantitative investigations of Li-S batteries. The need of such analytical tools is particularly crucial when applied to precipitation dynamics, which are a key limiting step to the sulfur utilization and rate performance of Li-S battery. Here, we conduct controlled experimentation to record the precipitation signatures for micro-electrodes and conventional porous electrodes for Li-S chemistry. We unravel how the polysulfide species, involved in the disproportionation reactions, control the peak shape and trends in the chronoamperometric profile of a sulfur electrode. This enables us to set the foundation for a new analytical framework for quantitative characterization of the precipitation mechanism in Li-S batteries.

1. Introduction

At first glance, lithium sulfur (Li-S) batteries appear to have several prohibiting characteristics that should render them unviable. Surprisingly, they proved not only viable, but ended up as a major frontrunner for the next generation of batteries[1–5]. Battery technologies that operate on conversion-based electrochemistry, like Li-S batteries, feature complicated (dis)charge mechanisms compared to the insertion-based lithium-ion batteries. The discharge of most Li-S systems presents two major voltage plateaus corresponding to two phases: the reduction of elemental sulfur to soluble polysulfides followed by the gradual precipitation of polysulfides to solid Li_2S. The core mechanisms of the conversions are based on chain-reactions featuring dissolution-precipitation, in which both the charge (S_8) and discharge precipitates (Li_2S) are electronically insulating and (near-)insoluble.[6–9] The hindering nature of the insulating precipitates complicates the further conversion of the sulfur and forces a reliance on a series of chemical interactions between the active species, solid and dissolved, a process called disproportionation. These interactions enable Li-S batteries to be reversible and kinetically viable. The disproportionation process is extremely difficult to characterize in all its fine details, and a few variations have been reported in the literature for different electrolyte formulations.[10–16] The reliance on polysulfides brings in major complications like the shuttle effect[17,18], the acceleration of anode degradation and the loss of active material[19,20], all of which plague the practical development of Li-S batteries.

Unlike lithium-ion batteries (LIBs), the quantitative reports are very limited in the Li-S literature[9,21–23], which are necessary to empirically establish and validate the thermodynamics and kinetics parameters of the sulfur electrodes.[24] The complex nature of the dissolution/precipitation steps in a Li-S battery renders the quantitative interpretation of its equilibrium and out-of-equilibrium signatures a very challenging undertaking. Particularly, unlike lithium ion batteries (LIBs), the (pseudo)equilibrium and dynamic characteristics of a sulfur electrode can be shown to be very sensitive to the cycling history, cycling path and the electrode design parameters such as the thickness, porosity, and formulation. This is briefly showcased in section 1.1 with the open-circuit-voltage (OCV) function of sulfur porous electrode. However, the further maturation and optimization of the materials for Li-S batteries can be accelerated with the help of the analytical tools provided that they are capable to accurately explain and quantify the (dis)charge mechanisms of the sulfur electrodes.

The unshakeable complexities of Li-S batteries are especially prominent during the precipitation of the Li_2S which has been identified as the key limiting step that determines the performance of Li-S batteries.[8,9,25–28] This step contributes up to 75% of the total discharge capacity while also acting as the rate-determining step and affecting the lifetime of the cell. In section 1.2, we provide a literature overview of the Li_2S precipitation mechanisms. Even though the kinetics of Li_2S precipitation are central to the energy and power density of a Li-S battery, there remains a lack of insight about it because tools that can probe it directly and locally are limited.[24] The crystallography and SEM/TEM are the main reliable techniques since Li_2S is a material that produces a very small signal for Raman, X-ray-based spectroscopy while NMR and other characterization techniques come with their own limitations.[9,14,16,23,29–31] With the help of some electro-precipitation formalisms like Bewick-Fleischmann-Thirsk (BFT) and Scharifker and Hills (SH) (section 2.1) chronoamperometry has been applied as an indirect characterization technique to probe Li-S batteries and gather quantitative insights about the Li_2S deposition.[9,24,32–40] However, it is often overlooked that such frameworks have been originally developed for other electrochemical systems with profound differences with Li-S batteries. The consequence is that those formalisms fail to quantitatively match the experimental chronoamperometry data to the Li_2S deposition behavior for Li-S batteries.

The main objective of the present study is twofold. First, to cast a critical look at the available reports on the chronoamperometry characterization of the Li_2S precipitation in lithium-sulfur batteries and expose the shortcomings and inconsistencies in using the classical analytical frameworks for this battery chemistry (section 2.2). Second, we propose and validate a physical picture and formalism that represent more accurately the Li-S system by considering its intrinsic complexities (section 2.4). We do so by experimenting the Li_2S precipitation on a variety of cell designs with different levels of idealization, most notably using a tailored-made microelectrode setup (section 2.3). All the information related to the different cells used in this study, including their exact composition and design, are gathered in the methods (section 4).

1.1. Peculiar behavior of Li-S batteries: open-circuit voltage and kinetics

In order to illustrate the hurdles involved with the characterization of a Li-S system, we have carried out a few fundamental characterization experiments. In **Figure 1a-b**, we compare the open-circuit-voltage (OCV) of two analogous Li-S cells recorded using three different techniques in common use for LIB, namely galvanostatic discharge at a very low C-rate, galvanostatic intermittent titration (GITT), and potentiostatic intermittent titration (PITT) techniques. The two Li-S coin cells contain sulfur electrodes of different thicknesses (10 vs. 90 µm), but are otherwise identical (see methods). We observe a significant difference among the OCV curves of the thin (Figure 1a) and thick (Figure 1b) sulfur electrodes. This is at odd with our expectation that the OCV function is an intensive property of an electrode material and must remain invariant to the loading and geometrical details of the electrode. Two major differences are noteworthy. First, the thicker electrode operates at slightly higher voltage and has a longer first-voltage plateau compared to the thinner electrode. Second, the OCV of thinner electrode exhibits an additional voltage plateau below 1.9 V vs. Li which is a manifestation of the reduction of the $LiNO_3$ electrolyte additive at the surface of the carbon in the sulfur electrode.[19] These differences cannot be solely explained by the porous-electrode-induced polarization effects. Instead, we believe that they mainly originate from the non-negligible impact of the extensive properties of the sulfur electrode such as sulfur loading and kinetics of polysulfides dissolution, disproportionation, and precipitation reactions. These transformations in Li-S batteries are never truly at rest even during the OCV conditions. Additionally, we observe differences among OCV techniques. Particularly, one needs to consider that the mobility of the polysulfide species in the electrolyte

leads to a 'junction potential'[41] In this regard, the OCV of a Li-S cell depends on the concentration profiles and transport properties of the electrolyte in addition to the energetics of the redox reaction of the cell. The sensitivity of the OCV to the E/S ratio and electrolyte additive were also investigated and presented in the supplementary information (**Fig S 17, 18, 19**) alongside a study case of a more practical cell design. The OCV from GITT is significantly higher than those obtained from PITT and low C-rate protocols. The difference starts off low during the first plateau, and widens for the second plateau. Such a protocol-induced variation in the OCV function can only result in the path-dependence and memory effects for sulfur electrodes. Those elements hinder significantly our ability to characterize Li-S systems consistently.

Just like the OCV establishment, the quantitative characterization of the reaction kinetics in a sulfur electrode is a big challenge on account of the multi-step and dissolution-precipitation nature of the discharge mechanism in Li-S batteries. Recent literature has shown some success in the application of Raman imaging in the quantification of the reaction kinetics for sulfur electrodes.[24] Here, we performed a series of in-situ operando Raman experiments on two analogous sulfur electrodes during a potentiostatic discharge in the first-plateau zone where the precipitation of the end-discharge product and passivation of the electrode is negligible. The only difference between the two electrodes is the use of a carbon-coated aluminum current collector for the sample labelled 'layered' in contrast to the 'bare' sample which uses a bare aluminum current collector (**Figure 1c-e**). The Raman images were analyzed (see **Fig S 20**) to obtain the effective dissolution coefficient (k_s) of the sulfur particles in the 2.2 – 2.3 V voltage window (**Figure 1d-e**). In the absence of solution-mediated reactions, one expects the sulfur particles to disappear at a rate linearly or exponentially proportional to the overpotential. Moreover, the presence of a conductive layer on the current collector decreases the contact resistance and hence increases the absolute value of overpotential for a given voltage, which in turns increases the reaction rate, of the reduction of sulfur.[42] However, the trends in the variation of reaction rate (k_s) as a function of voltage for our two sulfur electrodes deviate from the expected behavior (**Figure 1d**). Two observations are noteworthy. First, at the 'layered' electrode, the sulfur particles disappear at an almost similar rate at 2.3 and 2.25 V while a substantial faster kinetics is only observed when the voltage is lowered to 2.2 V. Second, at the 'bare' electrode, the sulfur particles disappear at a rate with a non-monotonic sensitivity to the voltage. Here, unlike the 'layered' sample, the k_s experiences a substantial increase when the voltage is lowered from 2.3 to 2.25 V, but thereafter slightly drops upon further decrease of voltage to 2.2 V. These unusual trends call for the contribution of non-electrochemical reactions in the effective rate of sulfur dissolution. For instance, the disproportionation reactions such as $S_8^{2-} \leftrightarrow S_6^{2-} + \frac{1}{4}S_8$ [26,43] can accelerate or decelerate the dissolution of sulfur particles depending on the evolution of the concentration of polysulfide species. This might explain the higher rate of sulfur dissolution at the bare electrode relative to the layered electrode at 2.25 V which is not expected if the charge-transfer at the electrode/electrolyte interfaces was the only reaction involving S_8. Generally, this experiment illustrates well the high sensitivity of the system due to small, uncontrollable parameters in the initial state of the system due to the path dependency and butterfly effect.

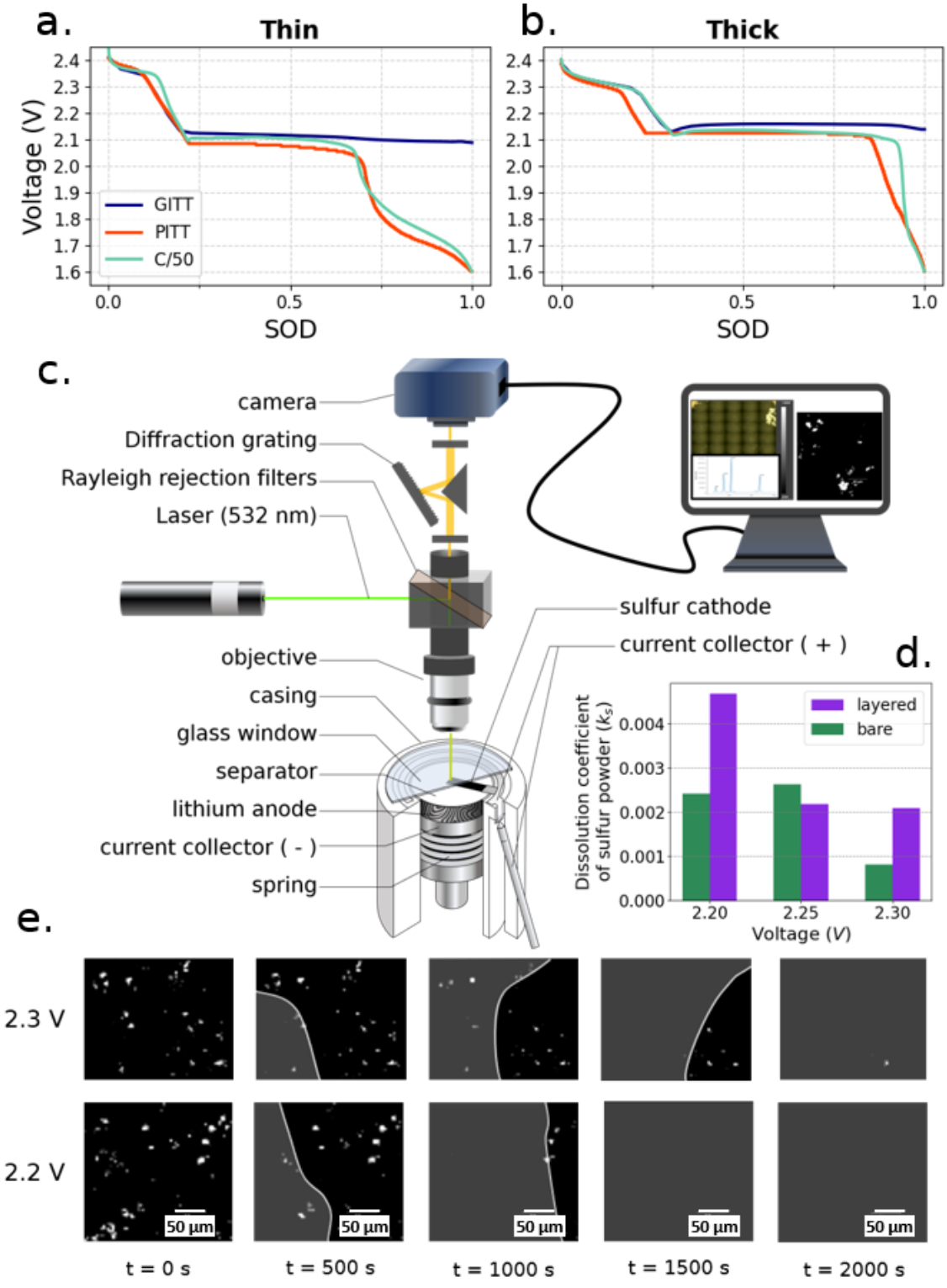

Figure 1. (a,b) *Open-circuit-voltage (OCV) profiles of sulfur electrode measured against Li electrode using three different techniques: GITT (blue), PITT (red) and low C-rate (green) discharge. The techniques were applied to cathodes with two different sulfur loadings:* ***(a)*** *1.40 mg/cm^2 (thick) and* ***(b)*** *0.10 mg/cm^2(thin).* ***(c)*** *Schematic of EL CELL and operando Raman confocal apparatus.* ***(d)*** *Dissolution rate of elemental sulfur during CV discharge based on* ***(e)*** *Raman mapping images of elemental sulfur (white) in the EL CELL cathode.*

1.2. A mechanistic overview of Li_2S precipitation

Early studies correctly identified that the Li_2S precipitate is insulating ($\sigma = 1 \times 10^{-9}$ to 1×10^{-13} S cm^{-1}) and insoluble. [8,44–47] A system with a single active species present in the electrolyte and with a precipitate sharing

those characteristics would theoretically not see its deposition layer grow in thickness. The conclusion of early studies is that Li_2S must precipitate as a one-nanometer-thin film which would then limit the cell capacity due to the passivation of the active surface area, i.e. the conductive substrate.[28,48] However, it was quickly demonstrated experimentally that Li_2S did not precipitate in a one-nanometer-thick films, but rather in films with thicknesses reaching up to 1 µm. Further empirical evidences demonstrated that 3D particles of comparatively large size (up to a few µm) could also be formed in the right conditions and take the form of spheres, flakes, spikes or other structures.[27,35,49–51][27,35,49–51] The first theory was no longer satisfying and other precipitation mechanisms had to be brought forward to explain the findings.

Currently, there are multiple complementing or competing mechanisms proposed in the literature to explain the precipitation of Li_2 which are summarized in **Figure 2a**. They can lead to two types of structures depending on the operating conditions (see **Table S 5**). In all cases, the first step involves a direct nucleation of one atom of Li_2S on an active site on the conductive substrate (**Figure 2a0**). From there, two paths branch out: the 2D-film and the 3D-particles growth. The 2D-film deposition is often considered undesirable due to its alleged quick passivation action. For the 2D-growth, two main mechanistic routes have been proposed: either Li_2S adatoms freely moving onto the active surface until their incorporation to an immobile nucleus, (**Figure 2a1, scenario 2D.A**) or the triple-interface deposition occurring at the intersection of active surface area, electrolyte and nuclei[8,28] (**Figure 2a3, scenario 2D.B**). However, it is worth noting that neither of these two mechanisms can explain how the thickness of 2D deposited films of insulating Li_2S invariably goes beyond the thickness of a monoatomic layer. This renders the entire 2D branch unsatisfactory. The 3D deposition path is generally considered as a more desirable path because it is associated to deeper discharge while leaving more active surface available for superior kinetics. For the 3D growth, two mechanisms are commonly proposed: either the desorption-redeposition[13,37,52,53] (**Figure 2a2, scenario 3D.A**) or the solution-mediated (disproportionation) deposition mechanism[13,27,28,54] (**Figure 2a4, scenario 3D.B**). The observed structures from experimentation range from flakes to spherical morphology[9,27,35,49–51] and present more complexity and variance beyond what the theoretical discussions let on.

In addition to the dimensionality of the precipitate, the analytical perspective involving the crystalline nature of the deposited Li_2S is noteworthy in the literature. Some papers have suggested that the deposited material can either be amorphous or crystalline. The former has been linked to 2D films, while the latter has been linked to 3D structures.[55] There exists some interesting variation to the main mechanistic routes presented in **Figure 2 a**. For instance, Prehal et al.[7] argue for the presence of Li_2S_2 as an intermediate species before converting to Li_2S. However, that variation still remains in essence close to the scenario 3D.A (**Figure 2 a2**). The impact and mere presence of Li_2S_2 and its role is debated in the literature because of its inconsistent visibility, which might be very sensitive to the system setting.[56]

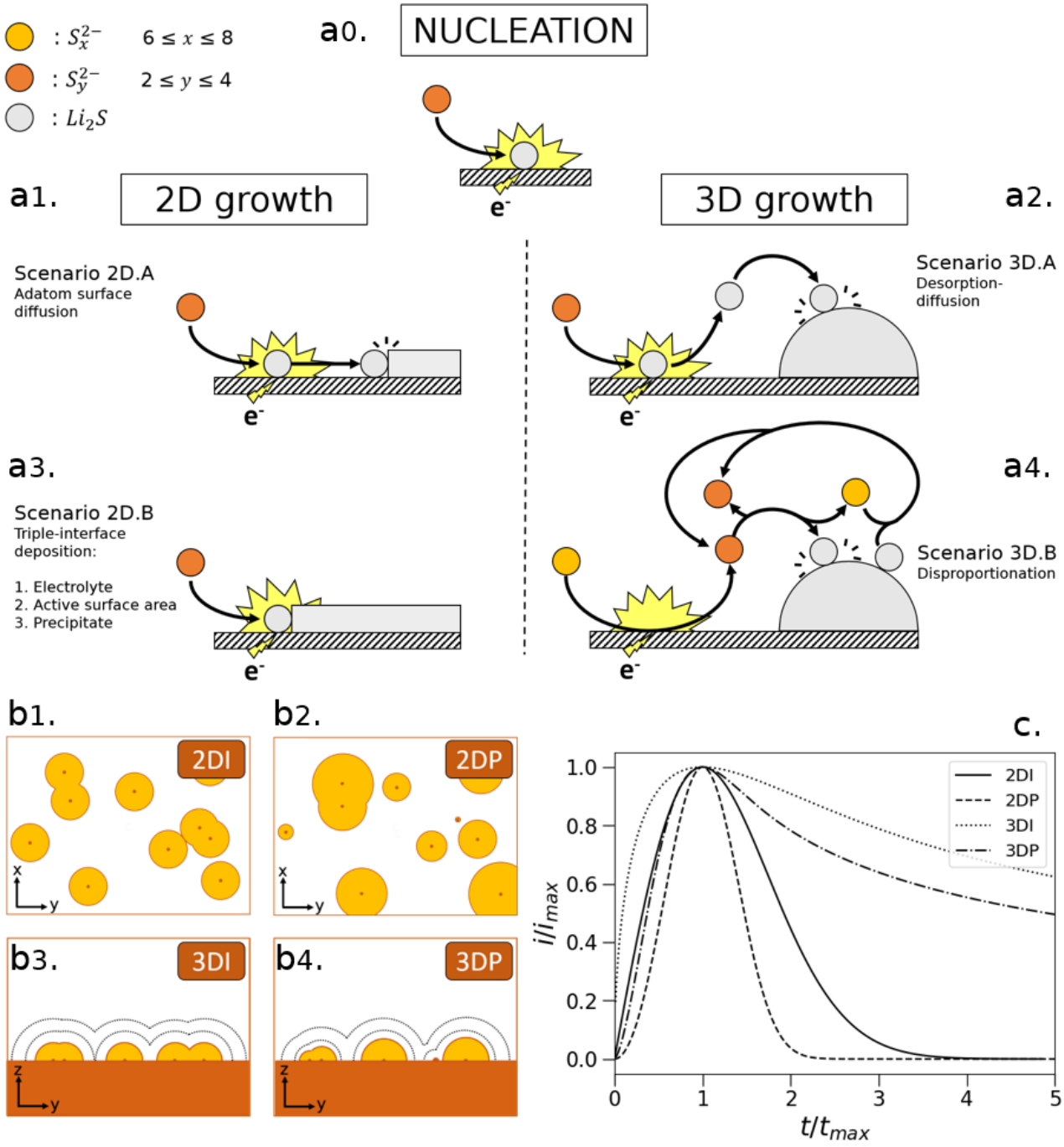

Figure 2. ***(a)*** *Schematic of the main different Li_2S precipitation routes as theorized in Li-S literature. All routes start with a nucleation step, but then each present specificities resulting in either a 2D or a 3D growth.* ***(b)*** *The different patterns of electrodeposition featuring in the classical deposition models. The nuclei can grow in 2D structures (atom-thick cylinder) or in 3D structures (hemispheres) and the nucleation step can occur instantaneously (2DI/3DI) or progressively (2DP/3DP) in time. In the former case, the growing nuclei all have the same size. In the latter case, there is a distribution of growing nuclei sizes.* ***(c)*** *The normalized current responses of an electrodepositing species in the four scenarios described in the classical deposition models.*

2. Results

2.1. BFT & SH formalisms for interpretation of chronoamperometric current-transients

In the context of electro-crystallization on a solid conductive substrate, there are four common physical pictures proposed in the literature: 2DI, 2DP, 3DI and 3DP.[57,58] These electrodeposition scenarios are categorized based

on the dimensionality of the precipitated and are either labelled "2D" (planar, **Figure 2 b1,b2**) or "3D" (hemispherical, **Figure 2b3,b4**). The electrodepositions are then further distinguished by "instantaneous" (I, **Figure 2b1,b3**) or "progressive" (P, **Figure 2b2,b4**) nucleation regimes. The 2DI-2DP models, also known collectively as the Bewick-Fleischmann-Thirsk (BFT) model[57] assume a lateral growth of precipitate on a flat surface, forming a film of a certain thickness. The rate-limiting step is assumed to be the incorporation of the adsorbed species to the lattice rather than the material transport to the reaction sites, i.e. a kinetic-limited scenario. More precisely, the model operates on the assumption that isolated two-dimensional nuclei grow in cylindrical monolayers with an expanding radius and a fixed height (**Figure S 27**). The 3DI and 3DP models known collectively as SH models were developed by Scharifker and Hills.[58] The SH model describes a system that is limited by material transport from the electrolyte to the active sites. The growth is therefore transport-limited and will be dictated by the diffusion of the dissolved species to the active sites rather than the conversion kinetics. The model works under the assumption that each nucleus grows as a hemisphere and therefore describes a case where 3D structures can form (**Figure 2b3,b4**). The chronoamperometry response of a system described by BFT or SH model features a current peak, originating from self-catalyzing growing nuclei surfaces that only get tempered as the nuclei begin to fuse with one and another or as the diffusion zones overlap (Avrami theorem). The current response will then tend to 0 as the remaining active surface area gets progressively passivated (**eq. S 44 & S 45**). The normalized BFT and SH expressions, **eq. S 50, S 51, S 69 and S 72**, are not sensitive to any parameter of the system and therefore can handily be compiled in a single plot (**Figure 2c**) which enables a quick visual check against the experimental chronoamperometry data to identify the dimensionality and growth regime for the passivation of a given electrode during electrodeposition.

2.2. Application to sulfur electrodes: shortcomings of BFT & SH frameworks

During a regular deep galvanostatic discharge of a Li-S battery, the initiation of the Li_2S deposition manifests as a voltage dip at the transition between the high- and low-voltage plateaus (see **Figure 1b** and **Fig S 21**). During a chronoamperometry (CA) test, the deposition of Li_2S creates a current transient featuring a peak. The physical interpretation of the increase, peak and subsequent decrease of the current response lies in the steps of the nucleation during discharge, as described in Wu et al.[51] In the initial stage of deposition, the growth of the surface nuclei leads to the incorporation of more precipitate per time interval, resulting in a current rise. Later on, two possible limiting scenarios curve back the trend: either the nuclei start to fuse together which limits the available surface for further precipitation or the concentration of active species in the liquid phase decreases too rapidly. In either or combined cases, the current reaches a peak and ultimately declines.

Figure 3a shows a non-exhaustive normalized CA plots compilation collected from the Li-S experimental literature together with the current-transient predictions of the BFT and SH models. Despite their normalization, the experimental CA curves are highly scattered in their behaviors, meaning they are sensitive to the testing conditions like the electrolyte formulation and the voltage. Therefore, they cannot be grouped neatly in one, or a handful of predictive curves, let alone fall in any of the BFT and SH model predictions. This is not surprising on account of the shortcomings of the models when applied to Li-S batteries. Indeed, the physical picture of the systems on which the models were built diverge significantly from the physical picture of Li_2S precipitation described in the section 1.2. **Table S 6** proposes a list of the diverging points. However, these models are still currently being extensively used in the Li-S reports to discuss the precipitation mechanisms.[24,32–40,59–61] Such reports either use a data presentation trick or perform an arbitrary data pre-treatment on the experimental current-transient data in order to force a partial match between the experimental data and the predictions of the BFT or SH models.[24] For instance, some reports limit the CA graph to a narrow frame around the peak.[34,37,51,59,60] Another example of data pretreatment would be the curve subtraction. We demonstrated that this method lacks any reliable working basis and therefore are not recommended (see **Fig S 28**). Simple deviation to the classical models can therefore not be ignored nor minimized with simplistic ad-hoc solutions.

Furthermore, we can occasionally observe glaring deviations to the models, mainly the presence of multi-peaks (often two) in the experimental current transients of Li-S batteries. Some examples from our own dataset are provided on **Fig S 22**, numerous other examples can be found in the literature[39,62–80] and a small compilation of them is shown in **Fig S 25**. In the BFT original paper[57], multi-peaks were addressed and explained as successive

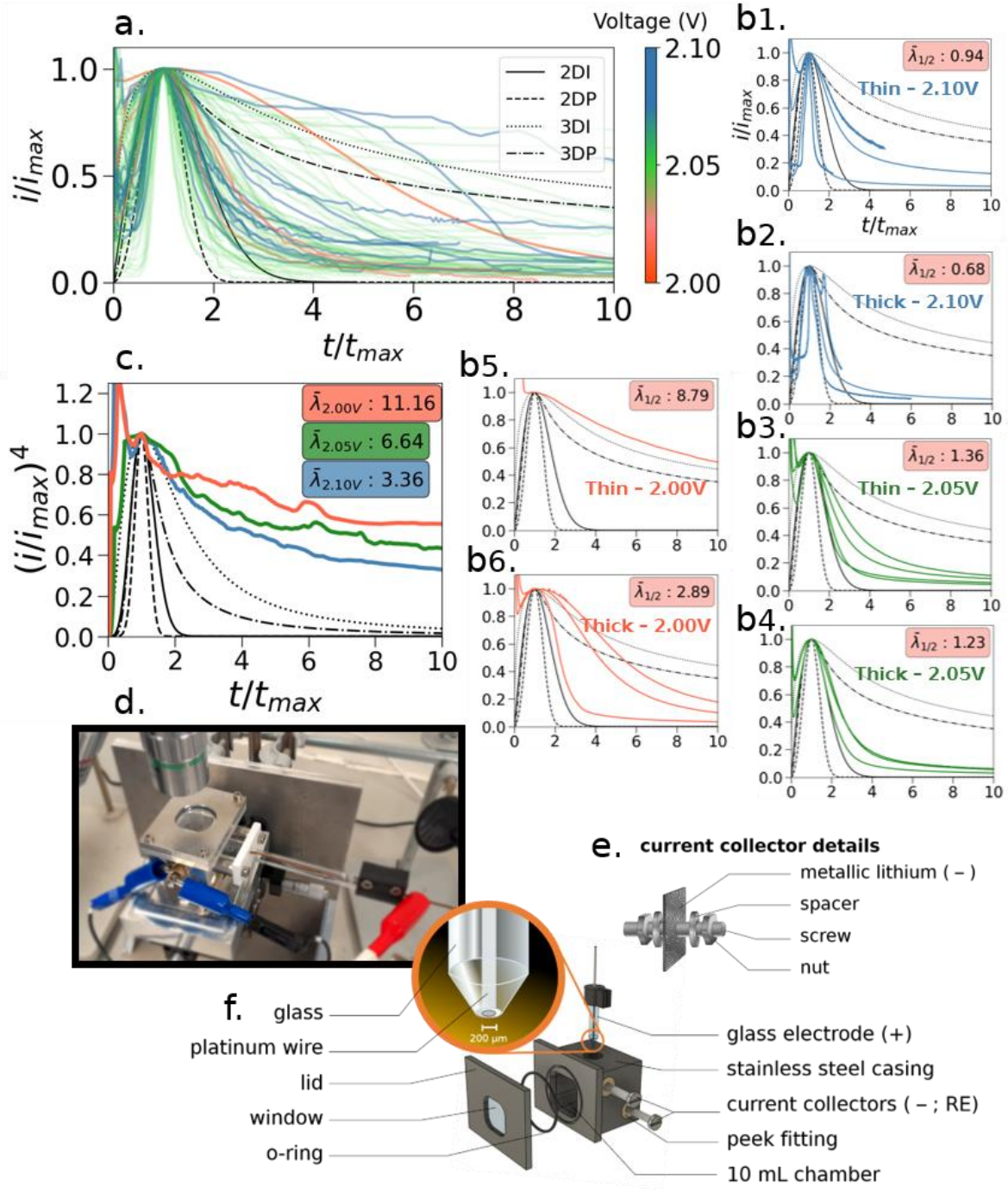

***Figure 3**. **(a)** Non-exhaustive compilation of the normalized chronoamperometry curves found in the literature[24,36–39,62–74,81–100] which illustrate a large diversity in behavior. **(b1-b6)** Chronoamperometry responses of cathodes in idealized and practical conditions. Two parameters were tested: coating thickness (thin: b2, b4, b6: 8 µm-0.1 mg_S/cm^2; thick: b1, b3, b5: 65 µm-1.45 mg_S/cm^2) and overpotential (b1, b4: 40 mV; b2, b5: 90 mV and b3, b6: 140 mV against the theoretical precipitation potential: 2.14 V). The thin coatings at 2.00 V hardly produced curves with any noticeable peak and therefore could not be systematically repeated. We suspect the peak to occur too early, when the current associated to long-chain polysulfides reduction is still dominant, drowning the precipitation signal. The variable "$\bar{\lambda}_{1/2}$" is used as a measure of the average width of the peaks and is defined in **Fig S 26. (c)** The chronoamperometric responses of **(d-f)** the tailor-made micro-electrode setup. The noise level observed in the current transients of the microelectrode originates from the very low current density (c.a. 400 nA). For clarity purposes, the measurement for each overpotential was recorded twice and then averaged. For the current transients of the microelectrode, $(I/I_{max})^4$ vs. t/t_{max} was plotted to accentuate the differences between the curves that would otherwise appear almost parallel.*

layer depositions, one after the other. In the Li-S system however, the insulating nature of Li_2S robs us of this explanation.

Those blatant discrepancies between the predictions and the observations did not go unnoticed in the literature and some explanations have been proposed. For instance, Wang et al.[38] argue that both the 3D and 2D deposition routes can occur simultaneously or in close succession, yielding superimposed current responses. Another group of reports suggest that the spatial-based heterogeneities in the sulfur electrode can explain the presence of multiple peaks in the CA data of Li-S batteries.[69,72,81] We performed some simple simulations (**Fig S 14**) to demonstrate that the porous-electrode effects can indeed lead to a variety of shapes for the current-transient profiles during a general phase-transformation reaction. The simulations demonstrate that a non-uniform distribution of the precipitation kinetics along the electrode thickness can result in the generation of current transients with multiple peaks (≥2), among other arbitrary shapes. In the next section, we investigated the deviation experimentally.

2.3. Chronoamperometric fingerprint of sulfur: from single particle to porous electrode

Here, we performed chronoamperometric tests on three different types of idealized electrodes, namely thin sulfur porous electrodes, bare aluminum substrate, and a microelectrode (3.14×10^{-4} cm^2 Pt disk). By comparing them to chronoamperometric responses of regular ('thick') cathodes, we aim at capturing the intrinsic current-transient signature of the sulfur in the absence of porous-electrode effects. Our hypothesis is that the existence of multiple active species, interacting through disproportionation, is the main driver of the observed diversity in the current transients reported in the experimental literature (**Figure 3a**) and their deviations from the conventional electro-precipitation models (BFT and SH). The impact of overpotential and electrode thickness on the current transient is presented in **Figure 3b**. The tests were carried out at 2.1V, 2.05V and 2.00V, corresponding to the overpotentials of 30 mV, 80 mV and 130 mV, respectively, assuming a theoretical precipitation potential of 2.13-2.14 V (see **Fig S 24**). The first observation is the diversity in curve behaviors within each tests, including all the tests performed on thinner electrodes (10 µm) for which the porous-electrode effects are minimal (**Figure 3b1,b3,b5**). The second observation is the systematic mismatch between all experimental curves and the predictions from the BFT and SH models. Noteworthy is the widening trend of the peaks when overpotential is increased. At lowest overpotentials, both the thick and thin electrodes exhibit current responses that cluster closer to the 2DP/2DI curves (**Figure 3b1,b2**), while at the highest overpotentials, the current transients cross over between 2DI and 3DP (**Figure 3b6**). At the intermediate overpotentials, most reported in the literature, the responses lie in between the two other groups (**Figure 3b3,b4**). The gradual widening of the curves with increasing overpotential does not follow the 3DP-3DI-2DP-2DI succession that is generally assumed in the literature.[35,101] This observation is experimentally is in line with previous reports.[24] We introduced $\lambda_{1/2}$, defined in **Fig S 26 a**, as a variable to quantify the width of the peaks at half-height. We notice a clear correlation between the mean peak width ($\bar{\lambda}_{1/2}$) and the overpotential (**Fig S 26 b**). The correlation between $\lambda_{1/2}$ and the thickness of electrode is uncertain because of the high standard error, but it strongly suggests that they are inversely correlated. Moreover, our dataset exhibited cases multi-peaks responses despite their uniform nature and their level of idealization (see **Fig S 22, S 23, S 24**).

The two most common hypothesis for peak broadening and multi-peaks should be discarded, namely the hypothesis based on independent deposition fronts for each different substrate within the cells, (e.g. carbon network, current collector, catalyst, etc.), or the hypothesis based on the steep concentration gradients within the electrode and electrolyte, i.e. porous-electrode effects. The former is unlikely as our chronoamperometric tests with a bare planar aluminum electrode within a catholyte solution (0.01 M Li_2S_8) did not exhibit any precipitation peak (**Fig S 27**), suggesting that the homogeneous carbon network is the only significant active surface for the precipitation of Li_2S. Likewise, we reject the hypothetic role of porous electrode effect as the source of model deviations because the widening trend and multi-peaks were both present in standard (thick) and idealized (thin and microelectrode) electrodes (**Figure 3b-c**, **Figure S 26 b**). Rather, we argue that the passivation of the idealized electrodes is slowed down through the disproportionation of the precipitates back into electrolyte, which is most prominent for the microelectrode within a flooded catholyte. In fact, we propose that disproportionation is the primary reason for the widening of the chronoamperometric peaks of the sulfur electrode. This hypothesis is validated in the next section with the help of a physics-based electrodeposition model.

2.4. A tailored electrodeposition formalism for Li-S batteries

Our proposed formalism for the electrodeposition in sulfur electrodes is based on a simple physical picture schematized in **Figure 4a**. Itfeatures one reversible disproportionation reaction (**R3,-R3**) and two reduction reactions (**R1** and **R2**). This picture can be considered as a combination of the routes 2D.B and 3D.B presented earlier (**Figure 2a**), which we argue to be more representative of the typical Li-S battery with the most common DOL:DME-based electrolytes. Of all the scenarios, 2D.B is the only one that unambiguously yields a current peak through the self-controlled deposition described by Avrami, and therefore fits into the BFT description with minimal changes, despite the fact that the BFT assumes conductive precipitate (**see Table S 6**). The common scenarios, 3D.A and 3D.B, only justify 3D deposition through electrolyte-mediated pathways: a desorption and re-precipitation route or the disproportionation route, respectively (**Figure 2a2,a4**), which is not encompassed in the classical models. The former is unlikely in most operating conditions of Li-S systems. In systems using the dominant electrolyte DOL:DME, the presence of S^{2-} or S_2^{2-} in the solution is disputed because they are not detected within classical measurement tools. The 3D.A scenario is thus unlikely or operating at neglectable kinetics. Therefore, we propose a new Li_2S deposition scenarios inspired by the scenarios 2D.B and 3D.B. Similar to BFT, we assume that the reactions are limited kinetically while the transport limitations are neglected. Contrary to the SH models, the 3D characteristic of the precipitate in the proposed model does not rely on conductive precipitate, but rather, is a direct consequence of the disproportionation pathway. Therefore, 2D and 3D growth co-exist, irrespective of the situation, and their contribution ratio is dictated by the kinetics of the disproportionation reaction (**R3**). All the assumptions involved in the development of the proposed model are listed in **Table S 2**.

$$Li_2S_8(aq) + 2e^- + 2Li^+(aq) \rightarrow 2Li_2S_4(aq) \quad \textbf{(R1)}$$

$$Li_2S_4(aq) + 6e^- + 6Li^+(aq) \rightarrow 4Li_2S(s) \quad \textbf{(R2)}$$

$$3Li_2S_8(aq) + 4Li_2S(s) \leftrightarrow 7Li_2S_4(aq) \quad \textbf{(R3)}$$

The reactions **R1** and **R2** correspond to the reduction of the active species, S_8^{2-} and S_4^{2-}, respectively, while reaction **R3** is a reversible disproportionation reaction. We explicitly distinguish between the growth of the nucleus linked to the direct electrodeposition (**R2**) and the dynamic disproportionation equilibrium occurring at the nucleus surface (**R3**). The **R2** is assumed to produce planar precipitate due to the fact that it is bounded to the triple-interface, while the dynamic **R3** is left solely responsible for the creation of 3D precipitate. Since the planar precipitate is only one atom thick, we can neglect its lateral surface contribution to the total surface of the nuclei. Parallelly, we assume that the lateral growth is only driven by **R2**, while the contribution of **R3** to the lateral growth can be neglected. The rate of surface passivation contributed by the direct electrodeposition (**R2**) is expressed following the original BFT model with the exception that we consider the growth coefficient to depend on the concentration of S_4^{2-} (**eq. S 5 & S 6**). The generation and consumption rate of species S_4^{2-}through **R3** reaction is considered to be proportional to the reaction drive (ϵ), defined as the out-of-equilibrium concentration for the S_4^{2-} and S_8^{2-} species, via an effective kinetic constant, k_3 **(eq. S 11 - S 13**). The final system of equations (**Table S 1**) was numerically solved to simulate the chronoamperometric current transients during the deposition of Li_2S in order to quantify the impact of the disproportionation reactions on the electrodeposition signature of Li-S batteries.

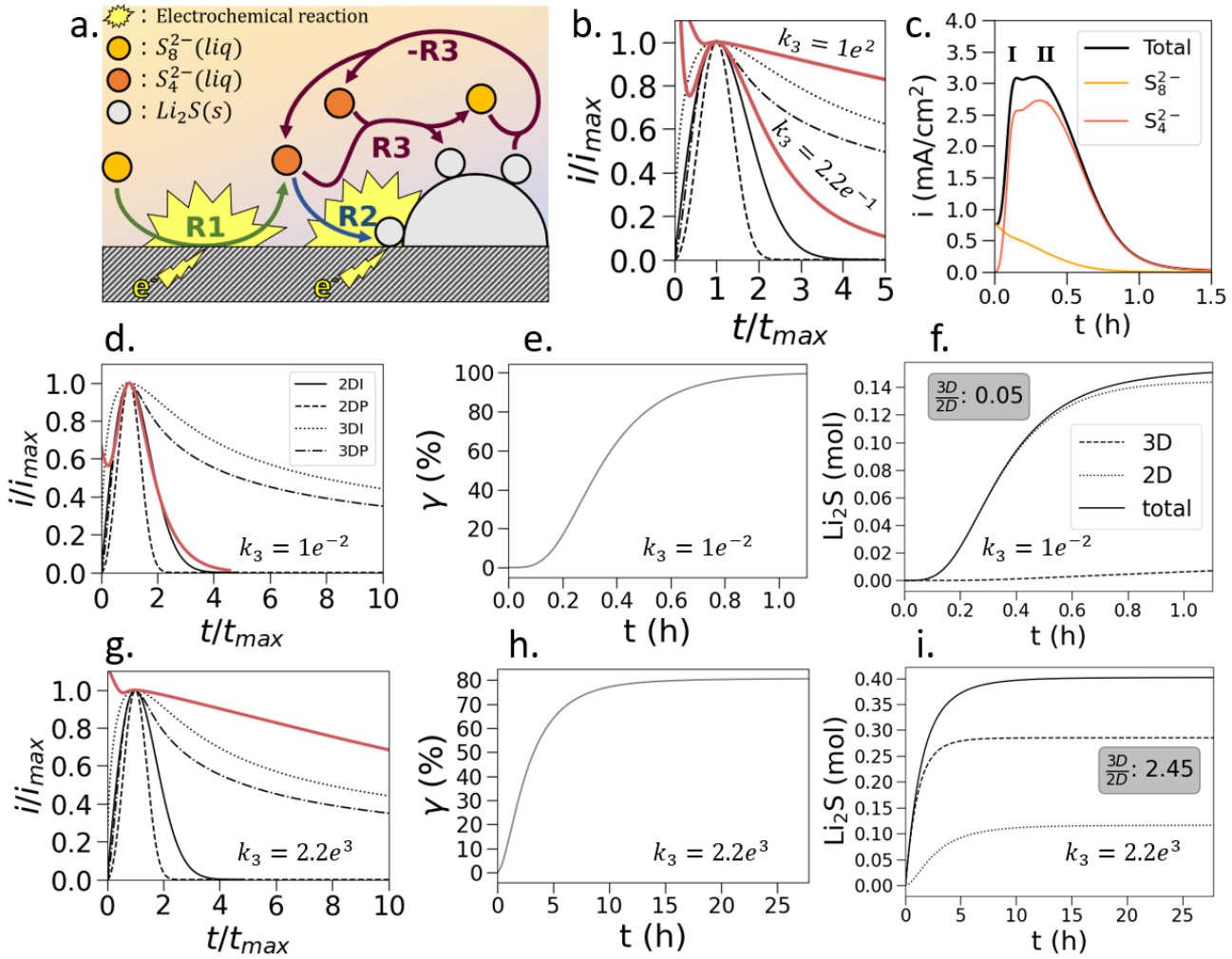

Figure 4. ***(a)*** *Schematic of the simplified deposition mechanism at the basis of the new formalism introduced in this work. The species involved consist in the dissolved polysulfides ('liq') and solid ('s') lithium sulfide. The three reactions, detailed in the text, consist in two irreversible electrochemical reactions (R1 and R2) occurring at the substrate/electrolyte interface and a reversible disproportionation reaction (R3 and -R3) occurring at the precipitate/electrolyte interface. The Li ions present in the electrolyte are not depicted for clarity purposes.* ***(b)*** *Sensitivity of the normalized chronoamperometric profiles to the rate constant of the disproportionation reaction (k_3),* ***(c)*** *a simulated current transient that features a double peak,****(d-i)*** *the simulations of chronoamperometric curves for two representative extreme cases of a very low* ***(d-f)*** *and high* ***(g-i)*** *value of k_3 in a cell with high polysulfide concentration (2 M). For both cases, are plotted:* ***(d,g)*** *the normalized current-time profiles,* ***(e,h)*** *the surface passivation,* ***(f,i)*** *the evolution of 2D vs. 3D growth. A parametrization table is provided in the supporting information for all simulations here presented (****Table S 4****).*

Our sensitivity analysis clearly shows that there is no universal and neat normalized current transient for the Li_2S precipitation like the ones suggested by the BFT and SH models (**Figure 4b**, **Fig S 8**). We find the rate constant of the disproportionation reaction **R3** (k_3) to be a crucial parameter in shaping the trend of the current transients. Particularly, the variation in k_3 can generate a whole series of chronoamperometric profiles with different broadness (**Figure 4b**) which would explain the diversity in the experimental current transients reported in the literature for Li-S batteries (**Figure 3a**). Higher values of k_3 tend to create very broad peaks while narrower peaks can be produced by lowering k_3. Further simulations reveal that the normalized response curve is also influenced by the initial bulk concentration of the polysulfides with a sensitivity that is highly dependent on the value of k_3 (**Figure 4d,g**). At low k_3 values, the impact of initial bulk concentration of polysulfides is minimal (**Fig S10** vs **Fig S11**), while at higher k_3 values, the impact becomes significant (**Fig S9.d3** vs **Fig. S13**). As such, the shape of the chronoamperometric peak is defined by the bulk concentration of the polysulfides and k_3, with a result of

broader peaks when both parameters are increased. This relation is reflected in our experimental data: the peaks gradually broaden as the catholyte-to-substrate (Cat/Sub) ratio increases. In **Figure 3**, the thick electrodes with the lowest Cat/Sub ratio present the narrowest peaks while the thin electrodes exhibit peaks of intermediate broadness and the flooded, flat-surfaced micro-electrode setup shows the broadest peaks. Cells with a higher Cat/Sub ratio tend to strongly favour the solvent-mediated reactions. This explains the higher values of k_3 refined for the flooded cells, although these cells have a lower bulk concentration of polysulfides (0.01 M) compared to the coin cells (0.05 M). The simulations produced diverse situations where both current contribution of **R1** and **R2** could display peaks (**Fig S 2**) and even one instance where **R2** produced a double-peak (**Figure 4c**). The ability of the model to generate multiple peaks confirms our earlier hypothesis that the appearance of extra peaks in the current transients is not necessarily a result of the porous-electrode effects (**Fig S 14**), but rather bespeak the complex interactions among the polysulfide species.

The passivation of the active surface area with the non-conductive precipitates is considered to be a major hinderance to the complete utilization of the sulfur loading in Li-S batteries. In this regard, the 3D growth of Li_2S is more efficient and can be promoted by the solution-mediated reactions, e.g. via use of redox mediators.[28,101] We showcased the flexibility of our formalism to reproduce the 3D growth at high electrolyte concentrations for the DOL:DME as a case study. Here, the kinetics of the **R3** reaction to resume equilibrium (k_3) represents the tendency of the disproportionation reaction (**R3**) to contribute in the precipitation of the 3D Li_2S in contrast to the planar passivation (**R2**). As such, the very low value of k_3 can lead to a premature end-of discharge due to a quick passivation of the active surface, $\gamma \to 1$ (**Figure 4d-f**). For instance, with $k_3 = 1e^{-2}$ cm.s^{-1}, the share of the 3D growth is less than 5% (**Figure 4f**), and the current transient closely coincides with the BFT 2DI classical model (**Figure 4d**). However, when the disproportionation has a faster kinetics ($k_3 = 2.2e^{3}$), the 3D growth can become a dominant route (>70%) for the precipitation of the end-discharge products (**Figure 4g-i**). Our own SEM analysis (see **Fig S 34**, **Fig S 35**) provides concrete evidences of 3D, spherical deposits, which have notable size differences between samples and a size distribution within the thicker cathode. We believe that more refinements of the experiments are likely to further solidify and exemplify the prediction of the model. In this regard, optimizing the cathodes to maximize polysulfide interactions or using strategies based on catalyst of the disproportionation are likely to be more productive than using strategies based on polysulfides immobilization. Under the former circumstances, a complete passivation of the active surface can be avoided (**Figure 4h**) which manifests in a chronoamperometric profile featuring a very broad peak and a current transient that tails off for a long time after the peak (**Figure 4g**). This behavior was very well showcased with the microelectrode (**Figure 3c-f**) and the ideal versus practical cell (**Figure 3b**) while being in a significant mismatch with the predictions of the classical models.

3. Conclusion

In this work, we demonstrated that the polysulfide interactions invalidate the blind application of common electrodeposition formalisms to Li-S batteries, where polysulfides effects are either neglected or subtracted as background noise. We proposed a new framework tailored for Li-S batteries which considers the polysulfide interactions and proved successful in producing a plethora of behaviors that are more representative of the field-observations, including complex and previously unexplained behaviors like multi-peaks during the chronoamperometry tests.

The findings of this work pave the road for more quantitative and in-depth characterization of the (dis)charge mechanism of the sulfur electrode as a function of electrolyte chemistry and electrode formulation. For instance, one can apply the analytical framework of this study to the systems with unconventional electrolytes such as those containing redox mediators or sparingly solvating electrolytes to shed light on the discharge mechanism and precipitation dynamics and hence accelerate the development of long-lasting Li-S cells. Moreover, the framework proposed in this study can be upgraded in the future works to accommodate more complexity regarding the polysulfides interactions, charge-transport limitations, progressive nucleation, and solid-solid conversion from Li_2S_2 to Li_2S. In addition to finer theoretical details, the formalism can also be expanded to more practical, i.e. complex, Li-S systems. For instance, one can include the effect of a catalyst, which is expected to alter the mechanistic details of the deposition as well as the morphology of the precipitate. It is important to investigate the possible sensitivity of the precipitation mechanism to the state-of-health of a sulfur electrode.

Therefore, the analysis of the long-term cycling data of a sulfur electrode using the modeling framework proposed in this study can be an interesting topic for a follow-up research. Finally, the mechanism of lithium sulfide dissolution and elemental sulfur deposition during charge are much less explored in the literature, but can be approached further using the analytical tools and framework developed in the present study.

4. Methods

Li-S cells assembly

For regular 2025 coin-cells used for the OCV measurements, we used an anode consisting in a metallic 23±1 mg Li punch of 15 mm, a separator (Celgard 2400) and a cathode, composed of elemental sulfur (Alfa Aesar, 60% weight ratio), carbon black C45 (Imerys, 32 % weight ratio) and polyvinylidene fluoride (PVDF, Solef, 8% weight ratio). The binder was prepared by mixing a 4% PVDF solution in N-methyl-2-pyrrolidone (NMP, Carl Roth, 99.8%) overnight at 55°C using a magnetic stirrer. The cathode coatings were made by blade casting (MSK-ASA-II) a slurry on an aluminum foil of 15.9±0.3 µm in thickness. The cathode slurry was mixed with NMP (1:4 weight ratio) using a centrifugal mixer (Kakuhunter SK-300S). The freshly coated cathodes were then placed in an oven (Thermo Scientific Heratherm) at 60°C overnight. The dried coatings were punched into disks of 12.8 mm diameter and their thickness and mass were measured. The cathodes labeled 'thick' had a dry thickness of 55 ± 3 µm and a loading of 1.40 ± 0.05 mg/cm^2, while the cathodes labelled 'thin' had a dry thickness of 12 ± 2 µm and a loading of 0.10 ± 0.02 mg/cm^2. The electrolyte was composed of lithium bis(trifluoromethanesulfonyl)imide (LTFSI, 1M), 1,3-dioxalane (DOL), 1,2-Dimethoxyethane (DME) and $LiNO_3$ (1% weight ratio). The two solvents had a 1:1 volumetric ratio. 55 µL of the electrolyte was added to the regular coin cells.

Some catholyte-based cells were assembled for the chronoamperometric tests. The assembly of catholyte coin cells was similar than those of regular coin cell except that the active material was not present in the dry cathode coating, but pre-dissolved in the electrolyte. The cathode coating was composed of carbon black C45 (Imerys, 80 % weight ratio) and polyvinylidene fluoride (PVDF, Solef, 20% weight ratio) in order to maintain the dry-surface-to-binder ratio constant. The cathodes labelled 'thick' had a dry thickness of 65 ± 5 µm and a loading of 1.44 ± 0.06 mg/cm^2, while the cathodes labelled 'thin' had a dry thickness of 8.0 ± 0.4 µm and a loading of 0.09 ± 0.03 mg/cm^2. The catholyte was prepared by mixing Li_2S (Thermo Scientific), S_8 (Alfa Aesar) in a 1:7 molar ratio in a 1M LiTFSI, DOL/DME (1:1 v) electrolyte at 60 °C for 48 h on a magnetic stirrer (300 rpm). 35 µL of the 0.05 M Li_2S_8 catholyte was added to the catholyte coin cells.

The EL CELL cells followed a similar assembly to regular coin cells, except that the cathode was either casted on regular aluminum current collector ("bare") of carbon-coated aluminum ("layered", one-sided 10±1 mg/cm^2). Then, instead of regular punches, the cathodes were shaped in rectangular slices of 1 mm x 5 mm rectangles using a scalpel blade and placed facing away from the lithium anode (see **Figure 1 a**). The end of the cathode was clamped to the current collector to ensure good electric contact. The loadings of the cathode were fixed at 1.55±0.04 mg/cm^2. Both the lithium anode and separator were punched into 10 mm diameter disks. 35 µL of 1M LiTFSI, DOL/DME (1:1 v) electrolyte was added to the cell.

Single-particle setup was tailor-made and composed of two metallic lithium (11 ± 1 mg) punches for both anode and reference electrode, a glass electrode with a 200 µm diameter platinum disk area as cathode and 10 mL of 0.01M Li_2S_8 catholyte. The cathode was cleaned before assembly by gently polishing its tip on sand paper (brand).

The metallic lithium anodes were prepared by gently polishing their surface with a scalpel blade right before assembly. All cells were assembled inside an argon-filled glovebox (Syllatec).

Operando confocal Raman microscopy characterization

Raman measurements were performed on a Renishaw inVia Qontor Raman microscope using a 50mW 532nm laser, a 2400l/mm grating and a Leica 50x long working distance objective (NA=0.50). Raman mapping data was acquired, centered around 210 cm^{-1}, using 1% laser power (0.5mW) and an exposure time of 50ms. Using the Renishaw WiRE software, cosmic rays were removed, and the baseline was subtracted. The Raman readings were synchronized with electrochemical sequences operated by a potentiostat (Ivium Vertex using IviumSoft software) through a Python script.

Electrochemical experiments

All coin cells were tested using a battery tester (Biologic BCS805). The home-made cell (homel) and the EL CELL were both operated with an Ivium Vertrex potentiostat. Four techniques were implemented: cycling, chronoamperometry (CA), galvanostatic intermittent titration technique (GITT) and potentiostatic intermittent titration technique (PITT). A 12 h rest was accorded to the freshly assembled cells for the wetting before any test. The cells undergoing CA were first initialized with a CV step at 2.15 V for 1h, then the CA was performed with 12h, 18h or 24h duration cut-offs for 2.00 V, 2.05 V and 2.10V set voltages respectively. Before the PITT, GITT and slow cycle, the cells were initialized with a single CCCV cycle at C/10 and 1 h rest periods. The GITT was conducted with 10 min pulses at C/10, spaced by 2h relaxation until the 1.6 V cut-off voltage. The PITT was conducted with voltage drops of 5 mV until the current reached 5 µA or 10h elapsed. Simple cyclings were performed at C/50. The upper and lower cut-off voltages were set at 2.8 V and 1.7 V respectively.

Modelling, data acquisition and processing

Comsol Multiphysics 5.6 was used to solve the equation systems, composed of PDEs with algebraic constraints. A Python algorithm, using the library mph, was used to loop through the parametrizations, launch the correspondent simulations, extract the data and create the plots. The data compiled from the literature, presented on **Figure 3 a**, was collected using Webplotdigitalizer 4, which can extract datapoints based on an image file. The examples in the literature are non-exhaustive and no systematic article selection process was applied. When the signal to noise was poor, we used the function *'smooth_data'* from the '*data_processing'* module in Python's library.

Statistical Analysis

A number of measurements were repeated to assess their variability, including cathode thicknesses, cathode loadings, Li anode weights, lambda values (characterizing peak broadness of chronoamperometric tests). Their average value '$\bar{x}$' was calculated using the arithmetic mean: $\bar{x} = \frac{1}{N}\sum_{i=0}^{N} x_i$ and the standard deviation 'σ' was calculated using the formula $\sigma = \sqrt{\frac{1}{N}\sum_{i=0}^{N}(x_i - \bar{x})^2}$. Such values were presented as ' $\bar{x} \pm \sigma$'. The sample size was set to minimum three in all case except mentioned otherwise. Concerning the comparison of the lambda values (see Fig S 26 b), a t-test was carried out to confirm that the variability of the measurements was too high to provide a definitive answer on the difference between thick and thin samples.

5. References

[1] X. Ji, L. F. Nazar, *J. Mater. Chem.* **2010**, *20*, 9821.

[2] Q. Pang, X. Liang, C. Y. Kwok, L. F. Nazar, *Nat Energy* **2016**, *1*, 1.

[3] S. Dörfler, H. Althues, P. Härtel, T. Abendroth, B. Schumm, S. Kaskel, *Joule* **2020**, *4*, 539.

[4] F. Duffner, N. Kronemeyer, J. Tübke, J. Leker, M. Winter, R. Schmuch, *Nat Energy* **2021**, *6*, 123.

[5] S. Yari, A. Conde Reis, Q. Pang, M. Safari, *Nat Commun* **2025**, *16*, 5473.

[6] S. D. Talian, G. Kapun, J. Moskon, A. Vizintin, A. Randon-Vitanova, R. Dominko, M. Gaberscek, *Chemistry of Materials* **2019**, *31*, 9012.

[7] C. Prehal, J.-M. von Mentlen, S. Drvarič Talian, A. Vizintin, R. Dominko, H. Amenitsch, L. Porcar, S. A. Freunberger, V. Wood, *Nat Commun* **2022**, *13*, 6326.

[8] F. Y. Fan, W. C. Carter, Y.-M. Chiang, *Advanced Materials* **2015**, *27*, 5203.

[9] L. Zhou, D. L. Danilov, F. Qiao, J. Wang, H. Li, R.-A. Eichel, P. H. L. Notten, *Advanced Energy Materials* **2022**, *12*, 2202094.

[10] M. Cuisinier, P.-E. Cabelguen, S. Evers, G. He, M. Kolbeck, A. Garsuch, T. Bolin, M. Balasubramanian, L. F. Nazar, *J. Phys. Chem. Lett.* **2013**, *4*, 3227.

[11] S. Waluś, C. Barchasz, J.-F. Colin, J.-F. Martin, E. Elkaïm, J.-C. Leprêtre, F. Alloin, *Chem. Commun.* **2013**, *49*, 7899.

[12] Y.-C. Lu, Q. He, H. A. Gasteiger, *J. Phys. Chem. C* **2014**, *118*, 5733.

[13] M. Cuisinier, C. Hart, M. Balasubramanian, A. Garsuch, L. F. Nazar, *Advanced Energy Materials* **2015**, *5*, 1401801.
[14] H. Wang, N. Sa, M. He, X. Liang, L. F. Nazar, M. Balasubramanian, K. G. Gallagher, B. Key, *J. Phys. Chem. C* **2017**, *121*, 6011.
[15] S. Waluś, C. Barchasz, R. Bouchet, F. Alloin, *Electrochimica Acta* **2020**, *359*, 136944.
[16] M. Sadd, S. De Angelis, S. Colding-Jørgensen, D. Blanchard, R. E. Johnsen, S. Sanna, E. Borisova, A. Matic, J. R. Bowen, *Advanced Energy Materials* **2022**, *12*, 2103126.
[17] Y. V. Mikhaylik, J. R. Akridge, *J. Electrochem. Soc.* **2004**, *151*, A1969.
[18] M. Fang, X. Liu, J.-C. Ren, S. Yang, G. Su, Q. Fang, J. Lai, S. Li, W. Liu, *npj Computational Materials* **2020**, *6*, 1.
[19] S. Zhang, *Electrochimica Acta* **2012**, *70*, 344.
[20] J. Castillo, J. A. Coca-Clemente, J. Rikarte, A. Sáenz de Buruaga, A. Santiago, C. Li, *APL Materials* **2023**, *11*, 010901.
[21] G. Zhou, H. Chen, Y. Cui, *Nat Energy* **2022**, *7*, 312.
[22] M. Zhao, B.-Q. Li, X.-Q. Zhang, J.-Q. Huang, Q. Zhang, *ACS Cent. Sci.* **2020**, *6*, 1095.
[23] S. Rehman, M. Pope, S. Tao, E. McCalla, *Energy Environ. Sci.* **2022**, *15*, 1423.
[24] S. Lang, S.-H. Yu, X. Feng, M. R. Krumov, H. D. Abruña, *Nat Commun* **2022**, *13*, 4811.
[25] C. Barchasz, J.-C. Leprêtre, F. Alloin, S. Patoux, *Journal of Power Sources* **2012**, *199*, 322.
[26] C. Barchasz, F. Molton, C. Duboc, J.-C. Leprêtre, S. Patoux, F. Alloin, *Anal. Chem.* **2012**, *84*, 3973.
[27] B. Yang, H. Jiang, Y. Zhou, Z. Liang, T. Zhao, Y.-C. Lu, *ACS Appl. Mater. Interfaces* **2019**, *11*, 25940.
[28] J. Sun, Y. Liu, L. Liu, J. Bi, S. Wang, Z. Du, H. Du, K. Wang, W. Ai, W. Huang, *Advanced Materials* **2023**, *35*, 2211168.
[29] L. A. Huff, J. L. Rapp, J. A. Baughman, P. L. Rinaldi, A. A. Gewirth, *Surface Science* **2015**, *631*, 295.
[30] A. Hoefling, D. T. Nguyen, P. Partovi-Azar, D. Sebastiani, P. Theato, S.-W. Song, Y. J. Lee, *Chem. Mater.* **2018**, *30*, 2915.
[31] A. Dorai, J. Kawamura, T. Omata, *Electrochemistry Communications* **2022**, *141*, 107360.
[32] Z. Li, H. Jiang, N.-C. Lai, T. Zhao, Y.-C. Lu, *Chem. Mater.* **2019**, *31*, 10186.
[33] R. Xiao, T. Yu, S. Yang, K. Chen, Z. Li, Z. Liu, T. Hu, G. Hu, J. Li, H.-M. Cheng, Z. Sun, F. Li, *Energy Storage Materials* **2022**, *51*, 890.
[34] D. Tian, X. Song, Y. Qiu, X. Sun, B. Jiang, C. Zhao, Y. Zhang, X. Xu, L. Fan, N. Zhang, *Energy & Environmental Materials* **2022**, *5*, 1214.
[35] Z. Li, Y. Zhou, Y. Wang, Y.-C. Lu, *Advanced Energy Materials* **2019**, *9*, 1802207.
[36] J.-L. Yang, S.-X. Zhao, Y.-M. Lu, X.-T. Zeng, W. Lv, G.-Z. Cao, *J. Mater. Chem. A* **2019**, *8*, 231.
[37] H. Chu, J. Jung, H. Noh, S. Yuk, J. Lee, J.-H. Lee, J. Baek, Y. Roh, H. Kwon, D. Choi, K. Sohn, Y. Kim, H.-T. Kim, *Advanced Energy Materials* **2020**, *10*, 2000493.
[38] Z.-Y. Wang, H.-M. Wang, S. Liu, G.-R. Li, X.-P. Gao, *ACS Appl. Mater. Interfaces* **2021**, *13*, 20222.
[39] J.-L. Yang, D.-Q. Cai, X.-G. Hao, L. Huang, Q. Lin, X.-T. Zeng, S.-X. Zhao, W. Lv, *ACS Nano* **2021**, *15*, 11491.
[40] L. Liu, Y. Meng, Y. Ge, D. Xiao, *ACS Appl. Mater. Interfaces* **2023**, *15*, 33525.
[41] J. Newman, K. E. Thomas-Alyea, *Electrochemical Systems*, John Wiley & Sons, **2004**.
[42] A. C. Reis, S. Yari, J. D'Haen, A. Hardy, N. Reddy, M. Safari, *Batteries & Supercaps* **2023**, *6*, e202300286.
[43] Q. Zou, Y.-C. Lu, *J. Phys. Chem. Lett.* **2016**, *7*, 1518.
[44] R. D. Rauh, K. M. Abraham, G. F. Pearson, J. K. Surprenant, S. B. Brummer, *J. Electrochem. Soc.* **1979**, *126*, 523.
[45] J. Shim, K. A. Striebel, E. J. Cairns, *J. Electrochem. Soc.* **2002**, *149*, A1321.
[46] Y. Yang, G. Zheng, Y. Cui, *Chem. Soc. Rev.* **2013**, *42*, 3018.

[47] Z. Lin, Z. Liu, N. J. Dudney, C. Liang, *ACS Nano* **2013**, *7*, 2829.
[48] N. A. Cañas, K. Hirose, B. Pascucci, N. Wagner, K. A. Friedrich, R. Hiesgen, *Electrochimica Acta* **2013**, *97*, 42.
[49] H. Pan, J. Chen, R. Cao, V. Murugesan, N. N. Rajput, K. S. Han, K. Persson, L. Estevez, M. H. Engelhard, J.-G. Zhang, K. T. Mueller, Y. Cui, Y. Shao, J. Liu, *Nat Energy* **2017**, *2*, 813.
[50] X. Wang, Y. Qian, L. Wang, H. Yang, H. Li, Y. Zhao, T. Liu, *Advanced Functional Materials* **2019**, *29*, 1902929.
[51] Z. Wu, M. Liu, W. He, T. Guo, W. Tong, E. Kan, X. Ouyang, F. Qiao, J. Wang, X. Sun, X. Wang, J. Zhu, A. Coskun, Y. Fu, *Nat Commun* **2024**, *15*, 9535.
[52] P. Andrei, C. Shen, J. P. Zheng, *Electrochimica Acta* **2018**, *284*, 469.
[53] H. Chu, H. Noh, Y.-J. Kim, S. Yuk, J.-H. Lee, J. Lee, H. Kwack, Y. Kim, D.-K. Yang, H.-T. Kim, *Nat Commun* **2019**, *10*, 188.
[54] L. Kong, J.-X. Chen, H.-J. Peng, J.-Q. Huang, W. Zhu, Q. Jin, B.-Q. Li, X.-T. Zhang, Q. Zhang, *Energy Environ. Sci.* **2019**, *12*, 2976.
[55] Z.-L. Xu, S. J. Kim, D. Chang, K.-Y. Park, K. S. Dae, K. P. Dao, J. M. Yuk, K. Kang, *Energy Environ. Sci.* **2019**, *12*, 3144.
[56] Z. Liu, P. P. Mukherjee, *ACS Appl. Mater. Interfaces* **2017**, *9*, 5263.
[57] A. Bewick, M. Fleischmann, H. R. Thirsk, *Trans. Faraday Soc.* **1962**, *58*, 2200.
[58] B. Scharifker, G. Hills, *Electrochimica Acta* **1983**, *28*, 879.
[59] Z. Guan, X. Chen, F. Chu, R. Deng, S. Wang, J. Liu, F. Wu, *Advanced Energy Materials* **2023**, *13*, 2302850.
[60] Y. Wang, H. Chen, W. Wu, J. Li, G. Zhang, C. Wei, S. Wang, L. Zhang, Y. Zheng, H. Li, *Chemical Engineering Journal* **2025**, *514*, 163405.
[61] L. Chen, J. Lai, X. Guan, H. Zou, J. Liu, L. Peng, J. Wang, Y.-P. Cai, Q. Zheng, *Angewandte Chemie International Edition* **2025**, *64*, e202423046.
[62] Y. Wang, R. Zhang, J. Chen, H. Wu, S. Lu, K. Wang, H. Li, C. J. Harris, K. Xi, R. V. Kumar, S. Ding, *Advanced Energy Materials* **2019**, *9*, 1900953.
[63] T. Wang, Y. Liu, X. Zhang, J. Wang, Y. Zhang, Y. Li, Y. Zhu, G. Li, X. Wang, *ACS Appl. Mater. Interfaces* **2021**, *13*, 56085.
[64] C. Wen, X. Du, F. Wu, L. Wu, J. Li, G. Liu, *ACS Appl. Mater. Interfaces* **2021**, *13*, 44389.
[65] K. Yuan, L. Yuan, J. Xiang, Y. Liao, J. Chen, Y. Huang, *ACS Appl. Mater. Interfaces* **2022**, *14*, 698.
[66] Y. He, Y. Luo, W. Zhang, S. Liu, K. Zhu, L. Huang, Y. Yang, X. Li, R. Yu, H. Shu, X. Wang, M. Chen, *ACS Appl. Mater. Interfaces* **2023**, *15*, 45915.
[67] S. He, J. Yang, S. Liu, X. Wang, X. Che, M. Wang, J. Qiu, *Chemical Engineering Journal* **2023**, *454*, 140202.
[68] X. Liu, L. Zhang, X. Ma, H. Lu, L. Li, X. Zhang, L. Wu, *Chemical Engineering Journal* **2023**, *454*, 140460.
[69] J. Liu, W. Gao, X. Zhang, J. Li, Q. Li, G. Li, Y. Zhang, Z. Chen, *Chemical Engineering Journal* **2023**, *471*, 144238.
[70] Q. Wang, B. Qin, Q. Jiang, B. Wang, Y. Chen, W. Yao, J. Qi, *Chemical Engineering Journal* **2023**, *476*, 146865.
[71] C. Xu, S. Zheng, J. Guo, D. Sun, Z. Zhang, J. Li, *Chemical Engineering Journal* **2023**, *463*, 142295.
[72] Q. Yang, X. Wei, X. Cao, L. Chen, L. Song, L. Kong, W. Sun, K. Xie, Y. Song, *Chemical Engineering Journal* **2023**, *452*, 139638.
[73] Z. Zhao, Z. Yi, Y. Duan, R. Pathak, X. Cheng, Y. Wang, J. W. Elam, X. Wang, *Chemical Engineering Journal* **2023**, *463*, 142397.
[74] Y. Guo, Z. Jin, J. Lu, L. Wei, W. Wang, Y. Huang, A. Wang, *Energy Environ. Sci.* **2023**, *16*, 5274.
[75] J. Wang, G. Li, D. Luo, Y. Zhao, Y. Zhang, G. Zhou, L. Shui, X. Wang, *J. Mater. Chem. A* **2021**, *9*, 11160.

[76] X. Liang, J. Cai, S. Qiu, S. Niu, Y. Liu, X. Wang, G. Wang, Z. Chen, M. Chen, *J. Mater. Chem. A* **2022**, *10*, 23780.
[77] W. Zhang, D. Hong, Z. Su, S. Yi, L. Tian, B. Niu, Y. Zhang, D. Long, *Energy Storage Materials* **2022**, *53*, 404.
[78] D. Yang, Z. Liang, P. Tang, C. Zhang, M. Tang, Q. Li, J. J. Biendicho, J. Li, M. Heggen, R. E. Dunin-Borkowski, M. Xu, J. Llorca, J. Arbiol, J. R. Morante, S.-L. Chou, A. Cabot, *Advanced Materials* **2022**, *34*, 2108835.
[79] H. Xu, G. Xu, S. Zhai, S. Jin, Y. Tong, Z. Kong, J. Li, H. Jin, H. Xu, *ACS Appl. Mater. Interfaces* **2023**, *15*, 58497.
[80] J. Wang, W. Qiu, G. Li, J. Liu, D. Luo, Y. Zhang, Y. Zhao, G. Zhou, L. Shui, X. Wang, Z. Chen, *Energy Storage Materials* **2022**, *46*, 269.
[81] Y. Zhao, Y. Gong, C. Gao, Z. Chen, C. Zheng, H. Lv, H. Wei, Z. Zhou, Y. Wang, *Chemical Engineering Journal* **2023**, *475*, 146229.
[82] J.-L. Yang, D.-Q. Cai, Q. Lin, X.-Y. Wang, Z.-Q. Fang, L. Huang, Z.-J. Wang, X.-G. Hao, S.-X. Zhao, J. Li, G.-Z. Cao, W. Lv, *Nano Energy* **2022**, *91*, 106669.
[83] C. Tian, B. Li, X. Hu, J. Wu, P. Li, X. Xiang, X. Zu, S. Li, *ACS Appl. Mater. Interfaces* **2021**, *13*, 6229.
[84] F. Li, M. Zhang, W. Chen, X. Cai, H. Rao, J. Chang, Y. Fang, X. Zhong, Y. Yang, Z. Yang, X. Yu, *ACS Appl. Mater. Interfaces* **2021**, *13*, 30746.
[85] B. Qin, Y. Cai, X. Si, C. Li, J. Cao, W. Fei, H. Xie, J. Qi, *ACS Appl. Mater. Interfaces* **2021**, *13*, 39424.
[86] Z. Wang, J. Lu, S. Li, Y. Guo, F. Lian, A. Wang, Z. Jin, W. Wang, *ACS Appl. Mater. Interfaces* **2021**, *13*, 58789.
[87] H. Xu, R. Hu, Y. Zhang, H. Yan, Q. Zhu, J. Shang, S. Yang, B. Li, *Energy Storage Materials* **2021**, *43*, 212.
[88] R. Wang, W. Tang, M. Tang, Q. Wu, J. Li, *ACS Appl. Mater. Interfaces* **2021**, *13*, 21544.
[89] C. Liang, S. Yang, D. Cai, J. Liu, S. Yu, T. Li, H. Wang, Y. Liu, H. Nie, Z. Yang, *ACS Appl. Mater. Interfaces* **2023**, *15*, 1256.
[90] F.-J. Liu, W.-L. Luo, Z. Zhang, J. Yu, J.-X. Cai, Z.-Y. Yang, *Chemical Engineering Journal* **2023**, *456*, 140948.
[91] J. Liu, M. Xue, Y. Zhou, S. Liu, T. Yan, *Chemical Engineering Journal* **2023**, *459*, 141556.
[92] M. Qu, Y. Bai, W. Yang, L. Peng, Z. Wang, W. Sun, K. Sun, *Chemical Engineering Journal* **2023**, *460*, 141723.
[93] K. Shi, Y. Sun, Z. Xiong, J. Li, H. Nan, Y. Lin, Z. Wei, Q. Liu, *Chemical Engineering Journal* **2023**, *460*, 141794.
[94] Z. Shi, T. Wang, Z. Shi, S. Cui, Z. Zhang, W. Liu, Y. Jin, *Chemical Engineering Journal* **2023**, *457*, 141264.
[95] J. Tian, Z. Shen, H. Cheng, X. Jin, Z. Li, Y. Wen, J. Hui, S. Guo, H. Zhang, Q. Zhu, *Chemical Engineering Journal* **2023**, *464*, 142541.
[96] W. Wang, X. Wang, J. Shan, L. Yue, Z. Shao, L. Chen, D. Lu, Y. Li, *Energy Environ. Sci.* **2023**, *16*, 2669.
[97] D. Zhao, Z. Xu, X. Yu, M. Chen, O. Wu, K. Zhou, W. Zhou, L. Ma, N. Wang, *Chemical Engineering Journal* **2023**, *474*, 145983.
[98] B. Wei, Y. Tu, Y. Xia, W. Theis, J. Zhang, Z. Xu, S. Chen, J. Chen, G. Yin, H.-L. Wang, *Chemical Engineering Journal* **2023**, *473*, 144887.
[99] C. Zhao, B. Jiang, Y. Huang, X. Sun, M. Wang, Y. Zhang, N. Zhang, *Energy Environ. Sci.* **2023**, *16*, 5490.
[100] W. Xia, Y. Chen, W. Wang, Y. Lu, Y. Chen, M. Chen, X. Yang, P. Gao, H. Shu, X. Wang, *Chemical Engineering Journal* **2023**, *458*, 141477.
[101] D.-Q. Cai, J.-L. Yang, T. Liu, S.-X. Zhao, G. Cao, *Nano Energy* **2021**, *89*, 106452.

Acknowledgements

The authors are grateful for financial support to FWO-Vlaanderen. A. Conde Reis and H. Hamed are PhD research fellow and junior Postdoc fellow (12A1R24N), respectively, of the Research Foundation Flanders (FWO Vlaanderen). The authors are also grateful for the work and contribution of Hilde Pellears concerning the preparation and measurements of the SEM samples.

Competing interests

The authors declare no competing interests.